Development/Plasticity/Repair

Balanced Enhancements of Synaptic Excitation and Inhibition Underlie Developmental Maturation of Receptive Fields in the Mouse Visual Cortex

Qi Fang,[1,2*] Ya-tang Li,[1*] Bo Peng,[1,2] Zhong Li,[1] Li I. Zhang,[1,3] and Huizhong W. Tao[1,3]

[1]Center for Neural Circuits and Sensory Processing Disorders, Zilkha Neurogenetic Institute, Keck School of Medicine, University of Southern California, Los Angeles, California 90033, [2]Neuroscience Graduate Program, University of Southern California, Los Angeles, California 90033, and [3]Department of Physiology and Neuroscience, Keck School of Medicine, University of Southern California, Los Angeles, California 90033

Neurons in the developing visual cortex undergo progressive functional maturation as indicated by the refinement of their visual feature selectivity. However, changes of the synaptic architecture underlying the maturation of spatial visual receptive fields (RFs) per se remain largely unclear. Here, loose-patch as well as single-unit recordings in layer 4 of mouse primary visual cortex (V1) of both sexes revealed that RF development following an eye-opening period is marked by an increased proportion of cortical neurons with spatially defined RFs, together with the increased signal-to-noise ratio of spiking responses. By exploring excitatory and inhibitory synaptic RFs with whole-cell voltage-clamp recordings, we observed a balanced enhancement of both synaptic excitation and inhibition, and while the excitatory subfield size remains relatively constant during development, the inhibitory subfield is broadened. This balanced developmental strengthening of excitatory and inhibitory synaptic inputs results in enhanced visual responses, and with a reduction of spontaneous firing rate, contributes to the maturation of visual cortical RFs. Visual deprivation by dark rearing impedes the normal strengthening of excitatory inputs but leaves the apparently normal enhancement of inhibition while preventing the broadening of the inhibitory subfield, leading to weakened RF responses and a reduced fraction of neurons exhibiting a clear RF, compared with normally reared animals. Our data demonstrate that an experience-dependent and coordinated maturation of excitatory and inhibitory circuits underlie the functional development of visual cortical RFs.

Key words: **development; excitation/inhibition balance; receptive field; synaptic input; visual cortex; whole-cell recording**

Significance Statement

The organization of synaptic RFs is a fundamental determinant of feature selectivity functions in the cortex. However, how changes of excitatory and inhibitory synaptic inputs lead to the functional maturation of visual RFs during cortical development remains not well understood. In layer 4 of mouse V1, we show that a coordinated, balanced enhancement of synaptic excitation and inhibition contributes to the developmental maturation of spatially defined visual RFs. Visual deprivation by dark rearing partially interferes with this process, resulting in a relatively more dominant inhibitory tone and a reduced fraction of neurons exhibiting clear RFs at the spike level. These data provide an unprecedented understanding of the functional development of visual cortical RFs at the synaptic level.

Introduction

High-quality visual function is progressively established during development, which depends on the concurrence of correct initial neural wiring and appropriately patterned sensory inputs (White and Fitzpatrick, 2007; Espinosa and Stryker, 2012; Cang and Feldheim, 2013; Hooks and Chen, 2020). This experience-dependent visual development is most prominent at the cortical level and peaks at the critical period (Berardi et al., 2000; Hensch, 2005; Trachtenberg, 2015), during which various important visual functionalities, including ocular dominance (Shatz and Stryker, 1978; Fagiolini et al., 1994; Hofer et al., 2006; Stephany et al., 2018), binocularity (Jenks and Shepherd, 2020;

Received Mar. 1, 2021; revised Sep. 14, 2021; accepted Oct. 23, 2021.

Author contributions: L.I.Z. and H.W.T. designed research; Q.F., Y.-t.L., B.P., and Z.L. performed research; Q.F. and Y.-t.L. analyzed data; and L.I.Z. and H.W.T. wrote the paper.

Y. Li's present address: Division of Biology and Biological Engineering, California Institute of Technology, Pasadena, California 91125.

This work was supported by Grants EY-019049 and EY-022478 to H.W.T. and Grant DC-008983 to L.I.Z. from the National Institutes of Health.

*Q.F. and Y-t.L. contributed equally to this work.

The authors declare no competing financial interests.

Correspondence should be addressed to Huizhong W. Tao at htao@usc.edu.

https://doi.org/10.1523/JNEUROSCI.0442-21.2021

Tan et al., 2020), orientation selectivity (Chapman and Stryker, 1993; White et al., 2001; Li et al., 2012; Moore and Freeman, 2012; Hoy and Niell, 2015), direction selectivity (Li et al., 2006, 2008; Rochefort et al., 2011; Clemens et al., 2012; Hoy and Niell, 2015; Smith et al., 2015; Roy et al., 2020) and binocular matching (Wang et al., 2010, 2015; Chang et al., 2020), are established, or refined and strengthened. Sensory deprivation such as dark rearing (DR) can affect the critical period and normal development of visual functionalities (Hubel and Wiesel, 1970; Shatz and Stryker, 1978; Fagiolini et al., 1994; Morales et al., 2002; Gianfranceschi et al., 2003; Wang et al., 2010; Li et al., 2012; Kang et al., 2013; Ma et al., 2013; Ko et al., 2014; Sarnaik et al., 2014; Jenks and Shepherd, 2020). Of all these visual functionalities, the spatial arrangement of ON/OFF receptive field (RF) is a major fundamental determinant (Hirsch and Martinez, 2006; Priebe and Ferster, 2012; Niell, 2015) as integration of individual sensory inputs from various visual field locations determines the response to the overall visual stimulation pattern. Importantly, the RF structure per se may undergo developmental changes, which in turn can instruct the refinement of other visual functions. However, research on the developmental evolution of RF structure in the visual cortex has remained limited (Braastad and Heggelund, 1985; Ko et al., 2013; Sarnaik et al., 2014; Hoy and Niell, 2015; Smith et al., 2017; Roy et al., 2020). Although a study of the developing mouse primary visual cortex (V1) has reported a slight shift toward more RF subunits and more elongated RFs over development (Hoy and Niell, 2015), how the synaptic input architecture underlying the spatial RF evolves during normal development and whether this process can be affected by sensory deprivation remains elusive.

To address these questions, in this study, we systematically examined both the spiking and synaptic RFs in layer 4 excitatory neurons of the mouse V1 during development with a repertoire of electrophysiological and modeling approaches. We found that significant maturation of spatially defined RFs occurred within 1 week after the onset of visual experience, which was accompanied by decreased spontaneous firing rates, increased evoked firing rates, and an enhancement of the signal-to-noise ratio (SNR) of visual responses. At the synaptic level, excitatory and inhibitory inputs were strengthened by a similar proportion, and the inhibitory subfield was enlarged in size over the same developmental period. In addition, we found that sensory deprivation by DR caused an apparently normal developmental strengthening of inhibition but an impedance of the broadening of the inhibitory subfield, whereas excitation paradoxically remained premature. The resulting abnormally dominant inhibition over excitation led to reduced response levels and smaller spike subfield sizes. Together, our data suggest that the balanced strengthening of excitation and inhibition contributes to the functional maturation of visual RFs during cortical development, which can be interfered with, at least partially, by sensory deprivation.

Materials and Methods

Animal preparation. All experimental procedures used in this study were approved by the Animal Care and Use Committee of the University of Southern California. C57BL/6J mice of both sexes, ages postnatal day (P)14–P17 for stage 1 (ST1) and P21–P28 for ST2, were used. For anesthetized preparations, animals were sedated with an intramuscular injection of chlorprothixene (5 mg/kg) and then anesthetized with urethane (1.2 × g/kg, i.p., at 20% w/v in saline), as previously described (Li et al., 2012, 2018). The level of anesthesia was confirmed by the lack of a toe pinch reflex, and additional urethane (0.2 × g/kg) was administered as needed. The body temperature of the animal was maintained at ~37.5° by a thermostatic heating pad (Harvard Apparatus). A tracheotomy was performed, and a small glass capillary tube was inserted to maintain a clear airway. A small craniotomy (~1 × 1 mm) was performed to expose the underlying V1, and the dura mater was partially resected. Warm artificial cerebrospinal fluid (ACSF) containing the following (in mM): 140 NaCl, 2.5 KCl, 2.5 $CaCl_2$, 1.3 $MgSO_4$, 1.0 NaH_2PO_4, 20 HEPES, and 11 glucose, pH 7.4, was applied to the exposed cortical surface when necessary. The eyes were covered with ophthalmic lubricant ointment until recording. During recording sessions, the eyes were rinsed with saline, and a thin layer of silicone oil (30,000 centistokes) was applied to prevent drying while allowing clear optical transmission. The eye movement and receptive field drift of single units were negligible within the recording time windows (Liu et al., 2010; Sarnaik et al., 2014).

For awake head-fixed preparations, a screw was glued to the skull surface of the mouse with acrylic dental cement under anesthesia with 1.5% isoflurane (v/v). The screw was clamped tightly with a metal headpost on the recording setup to achieve head fixation. After recovery from anesthesia, the mouse was trained to get accustomed to the head fixation and to run freely on a rotatable plate. On the day of recording, the mouse was again anesthetized with isoflurane and a craniotomy window was made over V1. A durotomy was further performed to allow the insertion of silicon probes. After the surgery, the exposed cortex was covered with a silicon elastomer (Kwik-Cast, World Precision Instruments). The mouse was fully recovered from anesthesia before recording sessions.

In vivo *electrophysiology.* Whole-cell voltage-clamp recordings were performed with an Axopatch 200B (Molecular Devices) following our previous studies (Li et al., 2012, 2018). The patch pipette had a tip opening of ~2 μm (4–6 MΩ). For whole-cell voltage-clamp recordings, we used a Cs^+-based intrapipette solution containing the following (in mM): 125 Cs-gluconate, 5 TEA-Cl, 4 MgATP, 0.3 GTP, 8 phosphocreatine, 10 HEPES, 10 EGTA, 2 CsCl, 1 QX-314, and 0.75 MK-801, pH 7.25. The pipette and whole-cell capacitance were compensated completely, and series resistance (25–50 MΩ) was compensated by 50–60% (at 100 μs lag). An 11 mV junction potential was corrected. Data acquisition scripts were custom developed with LabVIEW (National Instruments). Signals were filtered at 2 kHz for voltage-clamp recording and sampled at 10 kHz. The evoked excitatory and inhibitory currents were resolved by clamping the cell at −70 and 0 mV, respectively (Li et al., 2012; Liu et al., 2010). As discussed before, our blind whole-cell recording method highly biases sampling toward pyramidal neurons (Liu et al., 2009, 2010). For cell-attached loose-patch recordings, glass electrodes containing the ACSF were used. A 100–250 MΩ seal was formed on the targeted neuron. The pipette capacitance was completely compensated. Spikes were recorded under voltage-clamp mode, with a command potential applied to achieve a zero-baseline current. The spike signal was filtered at 10 kHz and sampled at 20 kHz. All neurons recorded in this study were located at a depth of 350–500 μm below the pia according to the microdrive reading, corresponding to layer 4, which was determined based on the distribution of genetically labeled layer 4 cells in the Scnn1a-Cre mouse (Li et al., 2012; Petrus et al., 2015).

For awake recordings, we used a 64-channel silicone probe (NeuroNexus), coated with DiI (1,1-dioctadecyl-3,3,3,3-tetramethylindocarbocyanine perchlorate, Invitrogen) to allow *post hoc* track recovery. The electrode was placed at an angle of 45° relative to the cortical surface and inserted to an appropriate cortical depth (~500 μm). After insertion, agarose was added to stabilize the electrode, and it was allowed to settle for 45 min. Signals were recorded by an Open-Ephys system at a 30 kHz sampling rate. Raw unfiltered traces were saved for off-line spike sorting and analysis.

Visual stimulation. Visual stimulation was generated with MATLAB (MathWorks) and presented on a 34.5 × 25.9 cm monitor (refresh rate 120 Hz, mean luminance ~41.1 cd/m^2) placed 0.25 m away from the right eye. A distance of 0.25 m from the mouse eye is equivalent to infinity (Liu et al., 2010). The center of the monitor was placed at 45° azimuth and 0° elevation, covering ±35° horizontally and ±27° vertically of the mouse visual field. Recordings were made in the monocular zone of the V1, contralateral to the stimulated eye. For forward mapping of RFs in anaesthetized conditions, flashing bright (57.5 cd/m^2) and dark (24.7 cd/m^2) squares (5 × 5° in size) were individually presented on a gray

background (41.1 cd/m^2) at different positions on an 11 × 11 grid according to a predetermined pseudorandom sequence. RFs were mapped for 5–10 repetitions. The stimulus duration was 200 ms, and the interstimulus interval was 240 ms. Spontaneous activity was determined by averaging spike rates during the interstimulus intervals when a gray background was displayed.

In awake recordings for forward RF mapping, small (5 × 5°) or large (10 × 10°) bright and dark squares were presented individually at different positions on the screen (stimulus duration = 200 ms, interstimulus interval = 240 ms, 5–10 repetitions). To map fine-scale RFs, sparse and dense noise stimuli, composed of static bright and dark squares (4 × 4°) were used for the spike-triggered average (STA; Hoy and Niell, 2015). Each stimulus pattern was presented for 32 ms (i.e., updated every other frame) without an interstimulus interval between consecutive patterns. RFs were consistently revealed by different stimulation methods (see Fig. 3*A*).

Data analysis. Spikes were sorted off-line. Spikes evoked by flashing stimuli were counted within a 70–270 ms time window after the stimulus onset. Stimulus-evoked spike rate (after subtracting the average spontaneous firing rate) was considered significant if it exceeded the average spontaneous firing rate by three SDs of baseline fluctuations. RF was identified as a spatially contiguous area within which multiple flashing squares evoked significant responses. The cells analyzed in this study had one ON (where bright squares evoked responses) and/or one OFF subfield (where black squares evoked responses). The signal-to-noise ratio was calculated as the ratio of the mean evoked firing rate within the dominant subfield over the average spontaneous firing rate.

To quantify the spatial properties of the two-dimensional ON and OFF subfields, we fit the hard boundary of the subfield with an ellipse (Liu et al., 2010; Li et al., 2018; Fang et al., 2020), and quantified the goodness of fitting by calculating the adjusted r^2. Only subfields that were well fitted ($r^2 > 0.9$) were considered to have a clear boundary. The radius of a circle with the same area of the fitted ellipse was determined as the size of the subfield. We measured the size for the dominant subfield (ON or OFF sign). Overlap index (OI) was calculated between the excitatory and inhibitory RFs of the same cell and defined as follows (Liu et al., 2010):

$$OI = \frac{W1 + W2 - d}{W1 + W2 + d},$$

where d is the distance between the peaks of two subfields, and $W1$ and $W2$ are the half widths on the inner side of the two subfields, respectively.

For voltage-clamp recording data, average excitatory and inhibitory response traces to flashing stimuli were first smoothed by averaging within a sliding 40 ms window. Excitatory and inhibitory synaptic conductance was derived according to the following equation (Liu et al., 2010; Li et al., 2012):

$$I(t) = G_r \times (V_m(t) - E_r) + G_e(t) \times (V_m(t) - E_e) + G_i(t) \times (V_m(t) - E_i).$$

$I(t)$ is the amplitude of current at any time point; G_r and E_r are the resting leak conductance and resting membrane potential, respectively; G_e and G_i are the excitatory and inhibitory synaptic conductance, respectively; $V_m(t)$ is the membrane voltage; and E_e (0 mV) and E_i (−70 mV) are the reversal potentials. $V_m(t)$ is corrected by $V_m(t) = V_h - R_s \times I(t)$, where R_s was the effective series resistance, and V_h is the applied holding voltage. Measurement of currents at two different voltages yielded a system of two equations that could be solved for G_e and G_i at any particular t. The peak synaptic conductance (subtracted by the baseline activity) was considered as the stimulus-evoked synaptic response. Similar to those in the loose-patch recording, synaptic ON and OFF subfields were defined as spatially continuous positions on which bright and dark squares evoked significant synaptic responses (i.e., averaged stimulus-evoked synaptic conductance above the baseline by 3 SDs of baseline fluctuation).

The awake recording data were processed as previously described (Chou et al., 2020; Fang et al., 2020). Recording sites in layer 4 were selected. For single-unit activity, the raw signals were filtered through a 300–6000 Hz bandpass filter. The spatially varying motion artifacts were removed by applying a common average referencing. The nearby four channels of the silicon probe were grouped as tetrodes, and semiautomatic spike detection and sorting were performed using the Plexon offline sorter. Clusters with isolation distance of >20 were considered separate clusters. Spike clusters were classified as single units only if the waveform SNR exceeded four (12 dB), and the interspike interval was longer than 1.2 ms for >99.5% of the spikes.

To determine the spatiotemporal RF, the spike train evoked by the sparse or dark-noise stimuli was reversely correlated with the stimulus sequence to derive the STA of the stimuli (Jones and Palmer, 1987; Fang et al., 2020). A 2D SD was calculated at each time lag from 0 to 200 ms as the strength of RFs. The RF showing the strongest response was used to determine the size of RF. The background response level was determined by averaging the spike numbers at the four borders of RF and subtracted from RF. The RF map was further divided by its 2D SD to obtain z scores. Pixel values with a z score <4 were set to 0.

Neuron modeling. A conductance-based single-compartment integrate-and-fire Neuron model (Liu et al., 2010; Li et al., 2012) was built with a neuron receiving excitatory and inhibitory synaptic inputs evoked by flash stimuli to simulate the membrane potential response, as follows:

$$V_m(t + dt) = -\frac{dt}{C}[G_e(t) \times (V_m(t) - E_e) + G_i(t) \times (V_m(t) - E_i) + G_r(t) \times (V_m(t) - E_r)] + V_m(t),$$

where $V_m(t)$ is the membrane potential at time t, C is the whole-cell capacitance, G_r is the resting leak conductance, and E_r is the resting membrane potential, set as −65 mV. E_e and E_i were set at 0 and −75 mV, respectively. C was set as 50 pF. G_r was calculated based on the equation $G_r = C \times G_m/C_m$, where G_m, the specific membrane conductance, is 10^{-5} S/cm^2, and C_m, the specific membrane capacitance, is 10^{-6} F/cm^2. Because previous studies in cortical pyramidal cells did not find drastic changes in intrinsic membrane properties including spike threshold after eye opening (Zhang, 2004), we assumed that the parameters defining membrane properties were constant between ST1 and ST2. The peak potential amplitudes above the resting membrane potential were quantified as postsynaptic potentials (PSPs).

The temporal profile of the evoked synaptic conductance was approximated by fitting the average waveform of synaptic response with an alpha function (Liu et al., 2010; Li et al., 2015, 2018), as follows:

$$G = G_{\max} \times (t - onset)/\tau \times e^{-(t-onset-\tau)/\tau}, \text{ for } t > onset,$$

with τ = 63 ms for the excitatory response and 83 ms for the inhibitory response. The onset of the inhibitory current was set at 5 ms after that of the excitatory current. $G_{\max}$, the peak amplitudes of the excitatory or inhibitory tuning curves, was determined from experimental data of the average peak synaptic conductance at ST1 and ST2. To simulate the enhancement of synaptic strength during development, we increased $G_{\max}$ from 1 ns to 7 ns for excitation and determined the $G_{\max}$ for inhibition according to a constant excitation to inhibition (E/I) ratio at 0.58. To simulate the effect of broadening of the inhibitory subfield during development, we systematically set the inhibitory subfield size to be the same or 5, 10, or 15° larger than that of the excitatory subfield while keeping the E/I at 0.58. To simulate the effect of dark rearing in preventing the developmental strengthening of excitation, we kept the inhibitory synaptic strength at ST2 and determined the excitation strength based on E/I ratio values ranging from 0.4 to 0.7. The peak amplitudes of the evoked synaptic conductances across spatial locations were derived from the spatial tuning curves approximated by a Gaussian function.

The peak firing rates were simulated by using a power law function (Carandini and Ferster, 2000; Li et al., 2015) as follows: $R(V_m) = k\lfloor V_m - V_r \rfloor_+^p$. R is the predicted firing rate, V_r is the resting membrane potential (−65 mV), k is the gain factor (6.2 ×

10^{-7}), p is the exponent, and + indicates rectification. V_r, k, and p were assumed to be constant during development. Because R is sensitive to variations of p, we chose a p value (5.3) to generate firing rates comparable to those experimentally observed. The predicted spiking subfield size was determined by the spatial range of PSPs above a 20 mV spike threshold. For the DR condition, we observed a significant reduction of spontaneous firing rates compared with NR mice (see Fig. 6*A*). Although it was not trivial to incorporate random spontaneous synaptic events in the neuron model, we simulated the effect of their reduction by an equivalent lowering of the spike threshold (to 17 mV). It should be noted that any differences in values from empirically observed data could be because of some unknown changes of parameters. For example, the physical spike threshold could be lowered after DR, which we could not examine during our experiments because of the Cs+-based internal solution used for voltage-clamp recording.

To model the dependence of detectability of RFs on spontaneous firing rate (see Fig. 6*J*), we used the mean spontaneous firing rate (±SD) from ST1 and ST2 data, respectively. We then generated a large pool of evoked firing rates for each testing SNR; the mean of the generated evoked firing rates within the pool was equal to the mean spontaneous firing rate times SNR, and the SD of the pool was selected based on experimental observations. We randomly sampled from the pool, and the sampled evoked firing rate was compared with the spontaneous firing rate. It was scored as detected if it was larger than the spontaneous firing rate by >3 SDs. For each SNR level, we performed 1000 trials and calculated a detection rate.

Statistics. The Shapiro–Wilk test was first performed to test the normality of the dataset. If the data were normally distributed, a parametric two-sample t test was applied. Otherwise, a nonparametric Wilcoxon rank-sum test was used. Fisher's exact test and χ^2 test were used to compare the ratios. Multiple comparisons were based on one-way ANOVA with *post hoc* tests with Bonferroni correction. The significance level of the tests was set as 0.05. Data were reported as mean ± SD, unless mentioned in the text. Statistical analysis was performed with MATLAB (MathWorks) and Prism (GraphPad).

Results

Maturation of spatial RFs in layer 4 of mouse V1

To understand developmental changes of visual RFs, we performed *in vivo* cell-attached loose-patch recordings in layer 4 of the mouse monocular V1 at different developmental stages (see above, Materials and Methods). Our recording paradigm has been proved to preferentially sample from excitatory pyramidal neurons (Liu et al., 2010; Li et al., 2012). The cells we recorded from were segregated into two groups according to the age of animals: within 3 d after eye opening (ST1, P14–P17, precritical period) and during the critical period for ocular dominance plasticity (ST2, P21–P28). The reason for us to choose these two stages is that several monocular visual selectivity features (e.g., orientation selectivity and linearity) mature significantly over 1 week after eye opening, in particular in layers 2–4 (Wang et al., 2010; Rochefort et al., 2011; Li et al., 2012; Ko et al., 2013; Hoy and Niell, 2015; Jenks and Shepherd, 2020). To map the ON and OFF subfields of the RF, we presented bright and dark squares (5 × 5°), respectively, flashing individually on the screen (Liu et al., 2009, 2010; Li et al., 2015). As shown by the poststimulus spike-time histograms (PSTHs) of an example neuron at ST1 (Fig. 1*A*), the response areas to the bright (ON) and dark (OFF) squares were not clearly distinguishable from the spontaneous activity and therefore neither an ON nor OFF subfield with a definite boundary could be defined. Indeed, the RFs of recorded cells at ST1 were mostly obscure or sluggish (33 of 41 cells; Fig. 1*B*,*C*), and only a small portion of the cells showed a spatially defined or clear RF (8 of 41 cells; Fig. 1*D*). In stark contrast, a typical neuron at ST2 exhibited a brisk burst of firing to the square stimulation, and a clear RF boundary could be delineated (Fig. 1*E*, green ellipse). Such spatially defined RFs were observed in the majority of cells recorded at ST2, with diversified spatial arrangements of ON/OFF subfields (Fig. 1*F*–*H*). This striking difference between the premature sluggish RFs at ST1 versus the clear RFs at ST2, and at adult ages as shown in our previous study (Liu et al., 2009), prompted us to study the functional maturation of visual cortical RFs during this critical developmental period when basic monocular response properties are refined (Hoy and Niell, 2015).

To better understand the nature of the RF development, we quantified RF properties of the cells at ST1 and ST2. We found that distributions of spontaneous firing rates of the cells at ST1 versus ST2 were greatly diverged, as the median value was 1.4 Hz at ST1 versus 0.41 Hz at ST2 (Fig. 2*A*, left). Accordingly, the mean spontaneous firing rate was significantly decreased at ST2 (Fig. 2*A*, right; $p < 0.001$, t test). On the contrary, the evoked firing rate (measured as the maximum within the RF) was significantly increased at ST2 (Fig. 2*B*; $p < 0.001$, t test). Because of these opposite changes of spontaneous and evoked firing rates, the SNR values of cells at ST2 were greatly enhanced compared with those at ST1 (Fig. 2*C*; $p < 0.001$, t test). The reduced spontaneous firing rate and enhanced SNR would allow neurons to better encode visual information. Indeed, while the cells at ST1 predominantly showed sluggish RFs; ~90% of ST2 cells (19 of 21) exhibited spatially well-defined RFs (Fig. 2*D*). Of cells showing clear RFs, 50% (4/8), 25% (2/8), and 25% (2/8) of ST1 cells had ON-OFF, ON-only and OFF-only RF types, respectively, whereas the fractions at ST2 were 37% (7/19), 26% (5/19), and 37% (7/19), respectively ($p = 0.79$, χ^2 test). All these RF types have been observed in layer 4 of the adult cortex (Liu et al., 2009). Interestingly, the size of the dominant subfield (ON or OFF sign) of those apparently precocious ST1 cells with clear RFs was similar to their ST2 counterpart (Fig. 2*E*; $p = 0.46$, t test). Overall, cells with clear RFs exhibited lower spontaneous firing rates than those with sluggish RFs (Fig. 2*F*; left, $p < 0.001$, t test). Even for the precocious ST1 cells, the rare cells with clear RFs tended to have lower spontaneous firing rates than those with sluggish RFs (Fig. 2*F*, right; $p = 0.094$, t test). These data indicate that the RF maturation is accompanied by a reduction of the spontaneous firing rate and enhancement of SNR.

It is possible that anesthesia has differential effects on circuits at different ages, contributing to the observed firing rate differences between ST1 and ST2. To avoid this confound, we further conducted extracellular multichannel recordings (with single-unit sorting) in awake mice at ST1 and ST2 (see above, Materials and Methods). We used different methods to map RFs, that is, forward mapping with singly flashed 5 and 10° squares, as well as sparse-noise and dense-noise mapping with STA (see above, Materials and Methods). As shown by three example cells (Fig. 3*A*), the different methods either consistently failed to reveal a spatially organized RF or revealed an RF at a similar location. The proportion of neurons exhibiting a clear RF greatly increased from ST1 to ST2 (Fig. 3*B*), and at ST2 it nearly reached the adult level (Fig. 3*B*, black column; see also Fang et al., 2020). Also consistent with data from anesthetized mice, there was a significant decrease in the spontaneous firing rate as well as an increase in the evoked firing rate and SNR (Fig. 3*C*–*E*). The SNR at ST2 was comparable to that at the adult level (4.83 ± 4.36, n = 27 cells, $p = 0.56$, t test; see also Fang et al., 2020). Consistent with data from anaesthetized animals, the size of the dominant subfield (measured with 5° squares) was not significantly

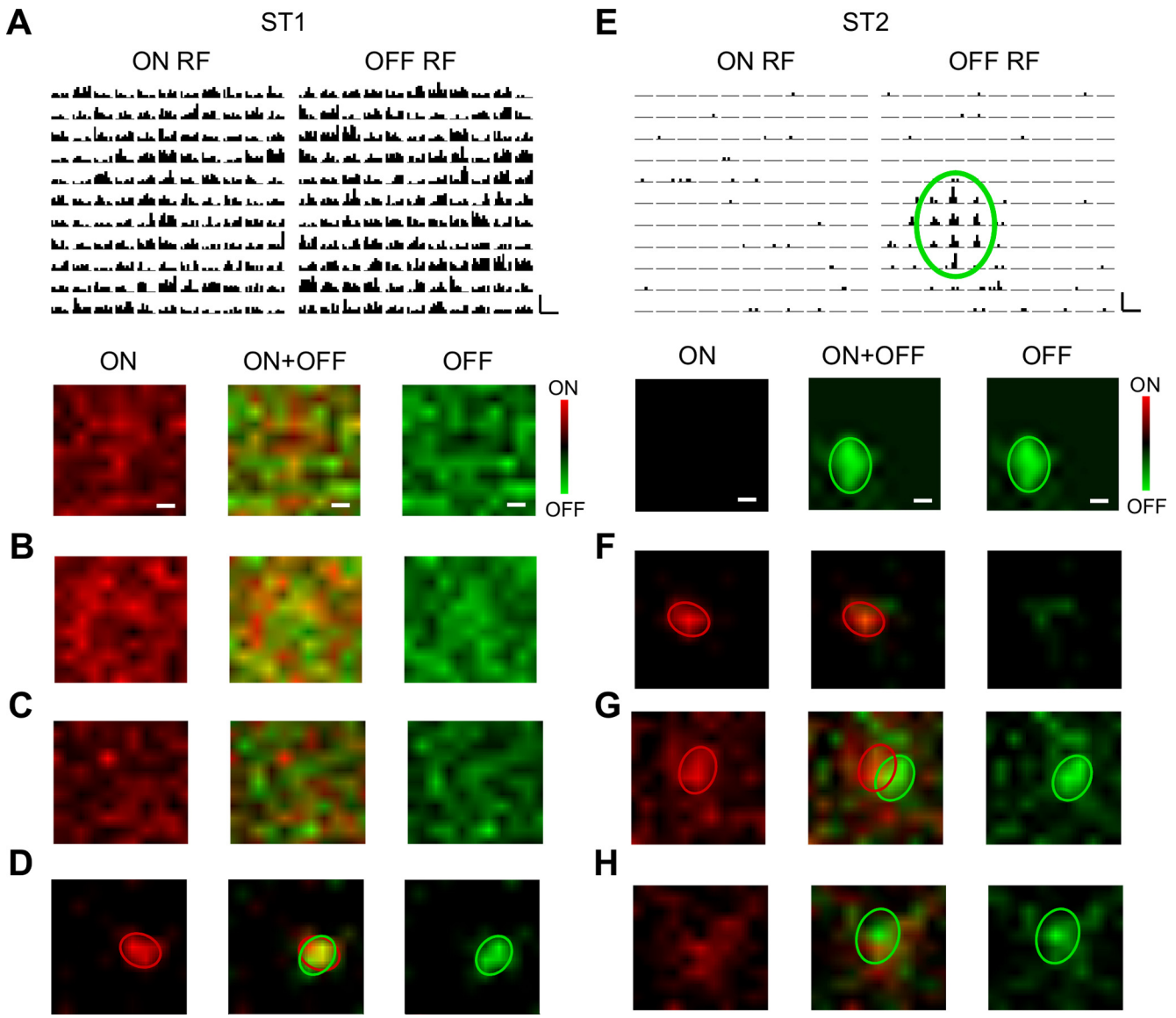

Figure 1. Developmental maturation of spatial RFs in mouse primary visual cortex. ***A***, One example layer 4 (L4) pyramidal neuron at ST1. Top, Plots of poststimulus spike time histograms (PSTHs) of its responses to bright (ON, left) and dark (OFF, right) squares (5 × 5°) presented at various locations. Scale bar, 5 Hz and 50 ms. Bottom, ON (left), OFF (right), and merged ON+OFF (middle) subfield maps of the neuron. The response strength is color coded. Scale bar, 5 Hz and 300 ms. Scale bar, 8°. ***B–D***, Three additional L4 pyramidal neurons at ST1. Red and green ellipses mark the boundary of defined ON and OFF subfields, respectively. ***E***, One example L4 pyramidal neuron at ST2. Data display is similar to ***A***. Top, PSTHs to bright and dark squares. Scale bar, 10 Hz and 50 ms. Bottom, ON, OFF, and merged subfield maps. Scale bar, 8°. ***F–H***, Three additional L4 pyramidal neurons at ST2.

changed from ST1 to ST2 (Fig. 3*F*). Together, these awake recording data further support the notion that maturation of monocular RFs mostly occurs between ST1 and ST2 and is characteristic of an enhancement of SNR.

Synaptic inputs underlying the developmental maturation of RFs

The reduction of spontaneous firing rates and popping out of clear RFs at ST2 are reminiscent of a general increase of inhibitory tone in the visual cortex during development, as reported in previous studies (Morales et al., 2002; Chattopadhyaya et al., 2004; Li et al., 2012). Thus, we sought to compare excitatory and inhibitory synaptic inputs underlying the spatial RF between ST1 and ST2. Because dense-noise mapping with STA tends to generate segregated ON/OFF subfields, although the underlying ON and OFF inputs could be overlapped (Fig. 3*A*, bottom), we chose to use forward mapping with sparse stimuli to better understand the spatial distribution of synaptic inputs. We performed whole-cell voltage-clamp recordings from layer 4 neurons and recorded excitatory and inhibitory synaptic responses to flashing bright and dark squares (5 × 5°) by holding the membrane potential at −70 and 0 mV, respectively (see above, Materials and Methods). No significant difference in input resistance was found between the recorded ST1 and ST2 cells (324 ± 78 MΩ vs 292 ± 57 MΩ, $p = 0.34$, t test, $n = 10$ and 12 cells, respectively). We observed that both excitatory and inhibitory synaptic responses were evoked by both ON and OFF stimuli in every cell recorded, even at ST1. As shown by an example neuron at ST1 (Fig. 4*A*), excitatory and inhibitory responses to ON and OFF stimuli (Fig. 4*A*, top) were spatially organized into largely overlapping excitatory and inhibitory ON/OFF subfields (outlined by blue and red ovals, respectively). To quantify the strength of synaptic responses, we deduced the synaptic conductance and measured the peak conductance after smoothing the conductance time

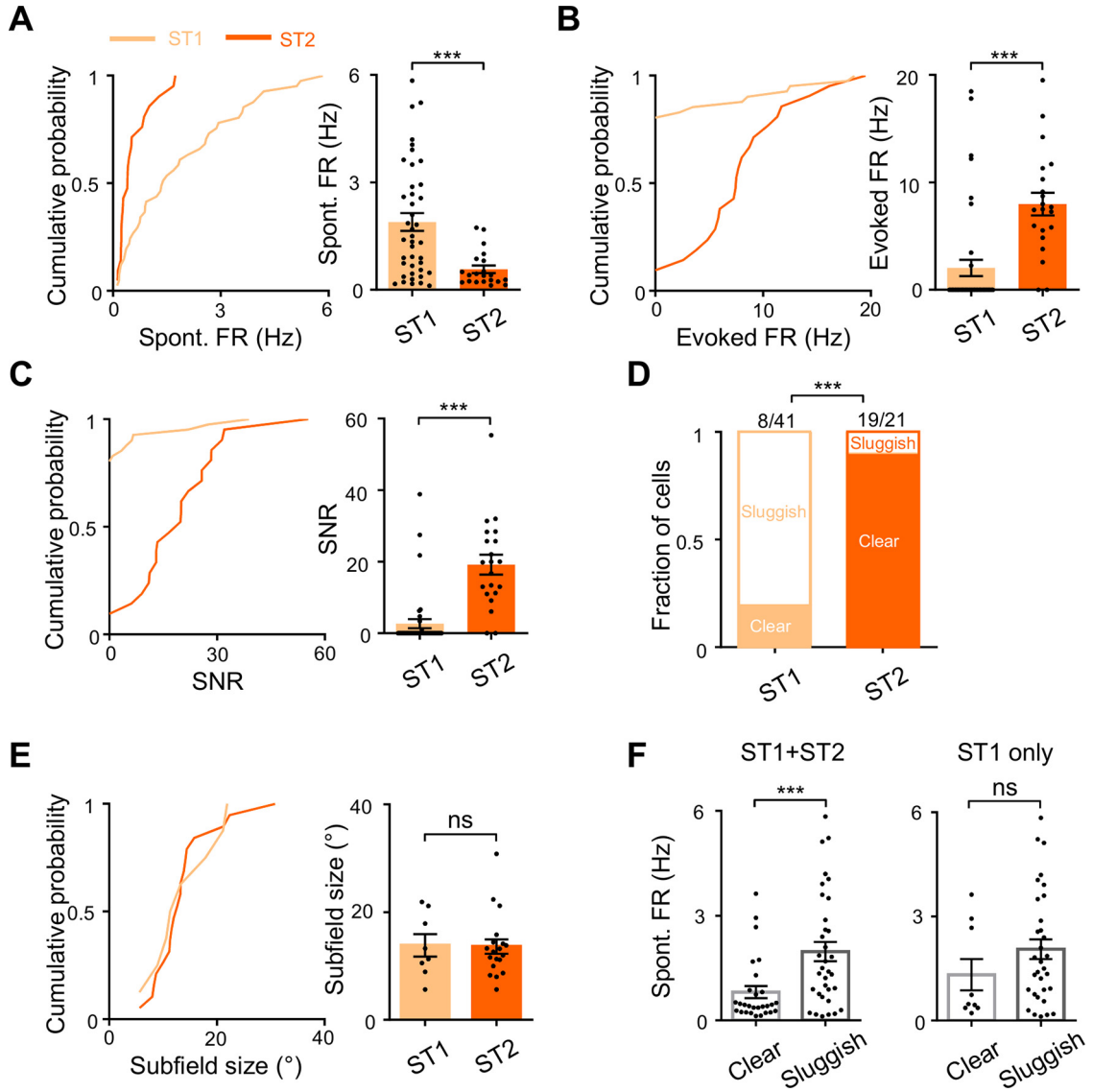

Figure 2. Summary of spike RF properties during development. ***A***, Left, Cumulative distribution of spontaneous firing rates of neurons at ST1 (light orange) and ST2 (dark orange), respectively. Right, Comparison of spontaneous rates at two stages (ST1, 1.9 ± 1.6 Hz (mean ± SD); ST2, 0.6 ± 0.5 Hz; ***$p < 0.001$, two-sample *t* test, $n = 41$ and 21 cells, respectively. ***B***, Comparison of evoked firing rates of neurons at ST1 versus ST2. ST1, 2.0 ± 4.9 Hz; ST2, 7.9 ± 4.8 Hz; ***$p < 0.001$, two-sample *t* test, $n = 41$ and 21 cells, respectively. ***C***, Comparison of the SNR of neuronal responses (ST1, 2.7 ± 8.0; ST2, 19.1 ± 12.5; ***$p < 0.001$, two-sample *t* test, $n = 41$ and 21 cells, respectively. ***D***, Fractions of clear versus sluggish RFs at ST1 and ST2; ***$p < 0.001$, Fisher's exact test, $n = 41$ and 21 cells, respectively. ***E***, Comparison of dominant subfield sizes (ST1, 13.8° ± 5.9°; ST2, 13.6° ± 5.8°, n.s., not significant, $p = 0.46$, two-sample *t* test; $n = 8$ and 19 cells, respectively. ***F***, Spontaneous firing rates of neurons with clear versus sluggish RFs. Left, All neurons at ST1 and ST2 are counted (Clear RF, 0.8 ± 0.9 Hz; Sluggish RF, 2.0 ± 1.6 Hz; ***$p < 0.001$, two-sample *t* test, $n = 27$ and 35 cells, respectively. Right, Only neurons at ST1 are counted (Clear RF, 1.3 ± 1.4 Hz; Sluggish RF, 2.1 ± 1.6 Hz; $p = 0.094$, two-sample *t* test, $n = 8$ and 33 cells, respectively. Error bar indicates SEM for all.

curve with a 40 ms sliding window (see above, Materials and Methods). The peak conductances evoked by ON and OFF stimuli at various locations were color coded to display the synaptic subfield maps (Fig. 4*A*, bottom). Similar to the example neuron in Figure 4*A*, in most of the neurons recorded at ST1 (8 of 10), we observed clear ON and OFF subfields for both excitatory and inhibitory inputs (Fig. 4*B*). This is evidently different from the spiking response data at ST1, where in most of the neurons no spatially clustered evoked responses were observed. At ST2, clear ON and OFF subfields could be identified for both excitatory and inhibitory inputs in every cell recorded (12 of 12; Fig. 4*C*,*D*). The arrangement of ON and OFF subfields at this stage appeared similar to that in ST1.

To quantitatively understand the progression of synaptic RF development, we compared two parameters, that is, synaptic strength (the maximum peak conductance within the RF) and subfield size (size of the subfield of the dominant sign), between ST1 and ST2. We found that strengths of both excitation ($p = 0.0097$, *t* test) and inhibition ($p = 0.0072$, *t* test) increased from ST1 to ST2 (Fig. 5*A*,*B*). The excitation-to-inhibition (E/I) ratio however remained the same (Fig. 5*C*; $p = 0.49$, *t* test), indicating that excitation and inhibition were enhanced by a similar proportion. Moreover, although the excitatory subfield size remained the same (Fig. 5*D*; $p = 0.31$, *t* test), the inhibitory subfield size significantly increased from ST1 to ST2 (Fig. 5*E*; $p = 0.019$, *t* test). Thus, the ratio of excitatory to inhibitory subfield size was significantly reduced (ST1, 1.01 ± 0.13; ST2, 0.87 ± 0.11; $p = 0.012$, two-sample *t* test; $n = 8$ and 12 cells). In addition, the spatial arrangement of largely overlapping excitatory and inhibitory subfields appeared similar between ST1 and ST2, as

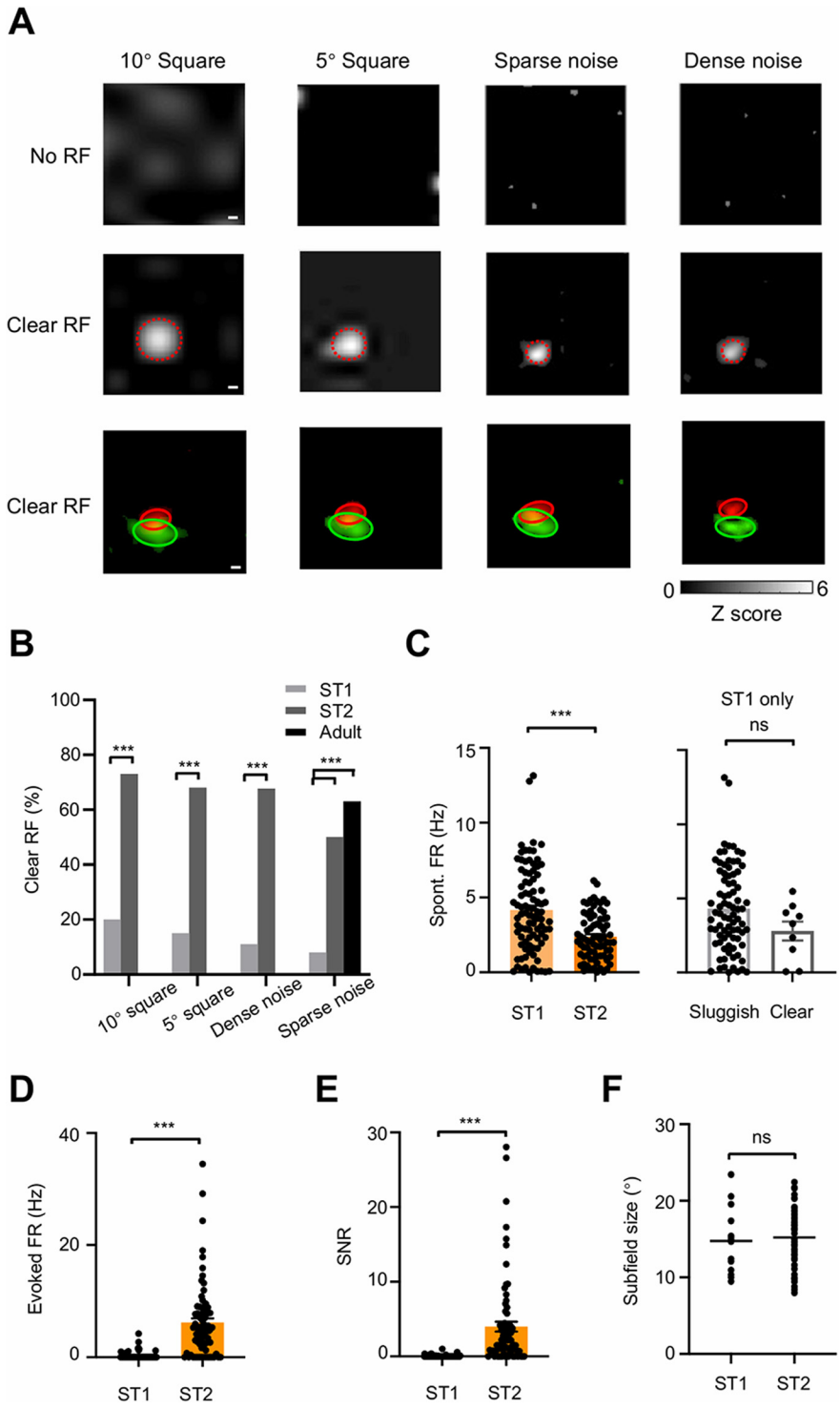

Figure 3. Development of spike RFs in awake mice. ***A***, Top, An example neuron without a clear RF when mapped with large (10° in size) or small (5° in size) flashing squares or sparse or dense noise. Middle, An example neuron with a clear and consistent RF of a single sign (ON), mapped with different sets of visual stimuli. The red dashed line marks the boundary of the RF. Bottom, An example neuron with an RF with both ON and OFF signs. Scale bar, 4°. ***B***, Summary of the percentage of neurons with a clear RF across developmental stages; ***$p < 0.001$, Fisher's exact test; $n = 85$ (ST1) and 75 (ST2) cells with 10° squares, 91 and 76 cells with 5° squares, 93 and 62 cells with dense noise, and 87, 62, and 51 (adult) cells with sparse noise. ***C***, Left, Comparison of the spontaneous rates of neurons at ST1 versus ST2 (ST1, 4.1 ± 2.8 Hz; ST2, 2.3 ± 1.5 Hz; ***$p < 0.001$, two-sample t test, $n = 91$ and 76 cells). Right, Spontaneous rates of neurons with and without a clear RF at ST1 only (2.8 ± 1.9 Hz and 4.3 ± 2.8 Hz, respectively; ns, significant, $p = 0.13$, two-sample t test, $n = 82$ and 9 cells). ***D***, Comparison of evoked firing rates of neurons (ST1. 0.3 ± 0.6 Hz; ST2, 6.2 ± 6.6 Hz; ***$p < 0.001$, two-sample t test, $n = 91$ and 76 cells. ***E***, Comparison of SNR values (ST1, 0.04 ± 0.14; ST2, 4.00 ± 5.75; ***$p < 0.001$, two-sample t test, $n = 91$ and 76 cells. ***F***, Comparison of subfield sizes (mapped with 5° squares; ST1, 14.7° ± 4.3°; ST2, 15.2° ± 3.8°; ns, not significant, $p = 0.68$, two-sample t test, $n = 14$ and 49 cells.

shown by the quantification of OIs (with 1 indicating complete overlap; Fig. 5*F*). Together, the changes of these synaptic RF parameters suggest that excitatory and inhibitory synaptic inputs are substantially strengthened during development, presumably contributing to the maturation of spike RFs. The spatially enlarged inhibitory RF may further help to sharpen and delineate the boundary of spike RF at ST2, similar to the function of broadened inhibitory orientation tuning in the sharpening of orientation selectivity at the spiking response level (Li et al., 2012).

The balanced enhancement of synaptic inputs leads to increased detection of RFs

To further understand how the balanced enhancement of excitatory and inhibitory synaptic inputs during development contributes to the observed changes in spike RFs, we used a single-compartment neuron model (Liu et al., 2011; Li et al., 2015) to simulate the membrane potential response resulting from the integration of synaptic excitation and inhibition evoked by each visual stimulus (see above, Materials and Methods). The temporal dynamics of the synaptic conductances was based on our experimental data (Fig. 6*A*, top). We kept the E/I ratio at 0.58 (the average E/I ratio of the recorded neurons across ST1 and ST2; Fig. 5C) and systematically changed the strength of excitation from 1 nano siemens (nS) to 7 nS (the range of excitatory input strengths across ST1 and ST2; Fig. 5*A*). That is, the strength of inhibition was also increased proportionally from 1.7 to 12.1 nS. As expected from our experimental data, we found that the peak amplitude of the simulated PSP response (Fig. 6*A*, bottom) monotonically increased as the strengths of synaptic inputs were proportionally enhanced (Fig. 6*B*,*C*, red dashed line).

To understand the direct effect of synaptic strengthening on RF development, we simulated one-dimensional subfields (of the same sign) of excitation and inhibition (Fig. 6*D*, inset), based on the average synaptic strengths observed at ST1 and ST2. By integrating the excitation and inhibition evoked at each spatial location, we then obtained PSPs at different locations and thus the subfield of PSP at ST1 and ST2 (Fig. 6*D*), assuming there were no changes in the synaptic subfield sizes. We found that the enhanced synaptic inputs at ST2 produced stronger PSPs than those at ST1, resulting in a pronounced spike

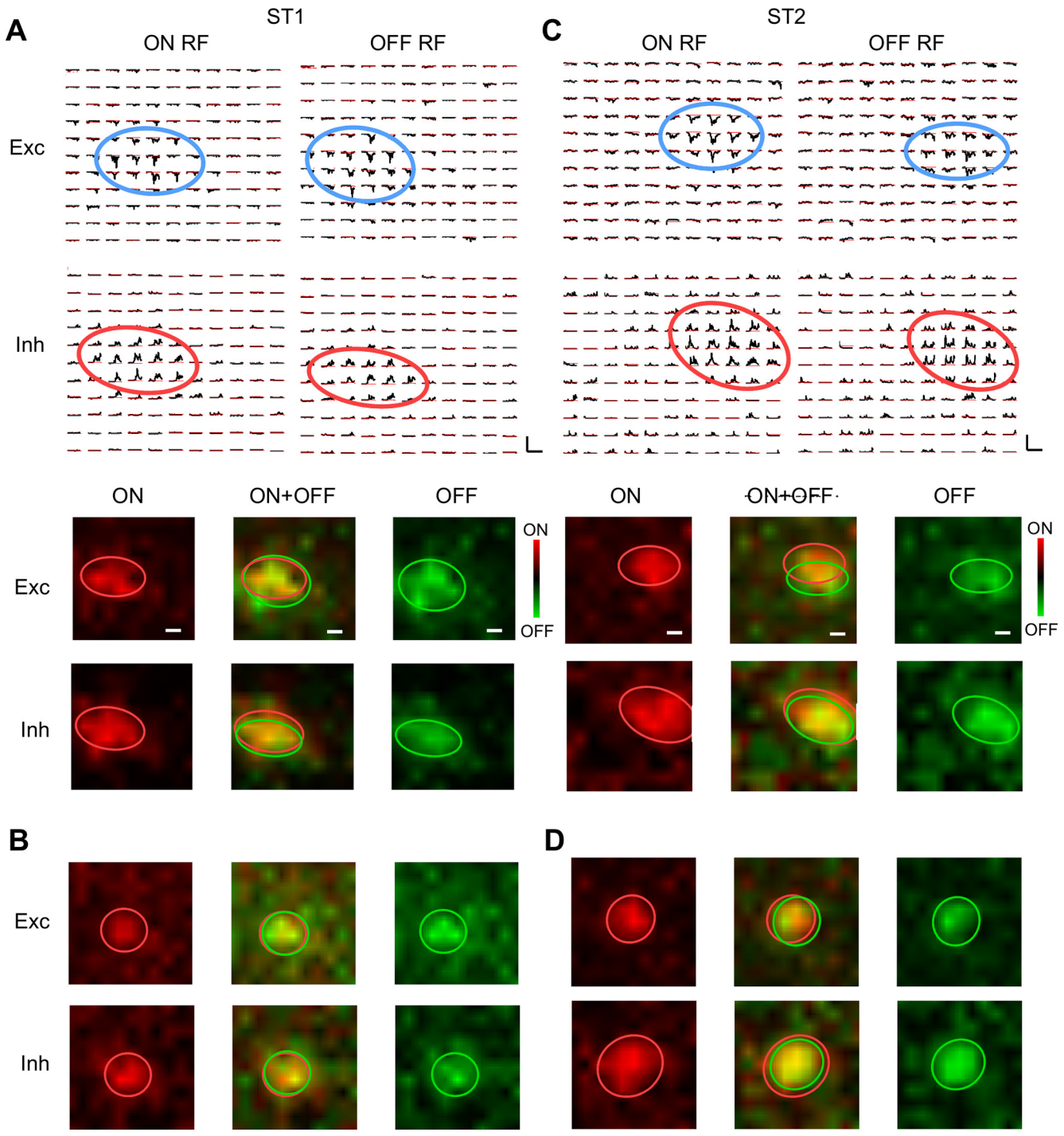

Figure 4. Synaptic inputs underlying developing RFs of layer 4 (L4) excitatory neurons. ***A***, Top, Averaged excitatory (Exc) and inhibitory (Inh) responses to bright (ON) and dark (OFF) squares (5 × 5°) for an example neuron at ST1. Blue and red ellipses mark the boundaries of the excitatory and inhibitory subfields, respectively. Scale bar, 250 pA, 300 ms. Bottom, Color maps of peak response amplitudes for excitatory and inhibitory ON (left), OFF (right), and merged (middle) subfields. Red and green ellipses delineate the boundaries of ON and OFF synaptic subfields, respectively. ***B***, An additional example neuron at ST1. ***C***, Excitatory and inhibitory subfields for an example L4 neuron at ST2. Scale bar, 300 pA, 300 ms. ***D***, An additional example neuron at ST2. Scale bar, 8° for all.

subfield above the presumed spike threshold (20 mV; see above, Materials and Methods). This indicates that the balanced enhancement of excitation and inhibition can directly contribute to the functional maturation of spatially defined spike RFs. Next, we systematically increased the maximum excitatory conductance within the RF from 1 nS to 7 nS while keeping the E/I ratio at 0.58 and predicted evoked firing rates based on the derived PSPs by using a power law function (Carandini and Ferster, 2000; Priebe and Ferster, 2012; Liu et al., 2011). As expected from PSPs, the spike subfield appeared only above a certain threshold conductance value (~3 nS), and after that the peak firing rate and the spike subfield size increased with increasing synaptic strengths (Fig. 6*E*,*F*). When we further enlarged the inhibitory subfield as observed for ST2, the increase in spike subfield size was then largely limited (Fig. 6*F*, red).

Next, using a similar modeling approach, we predicted the peak PSP within the RF for each recorded neuron by integrating

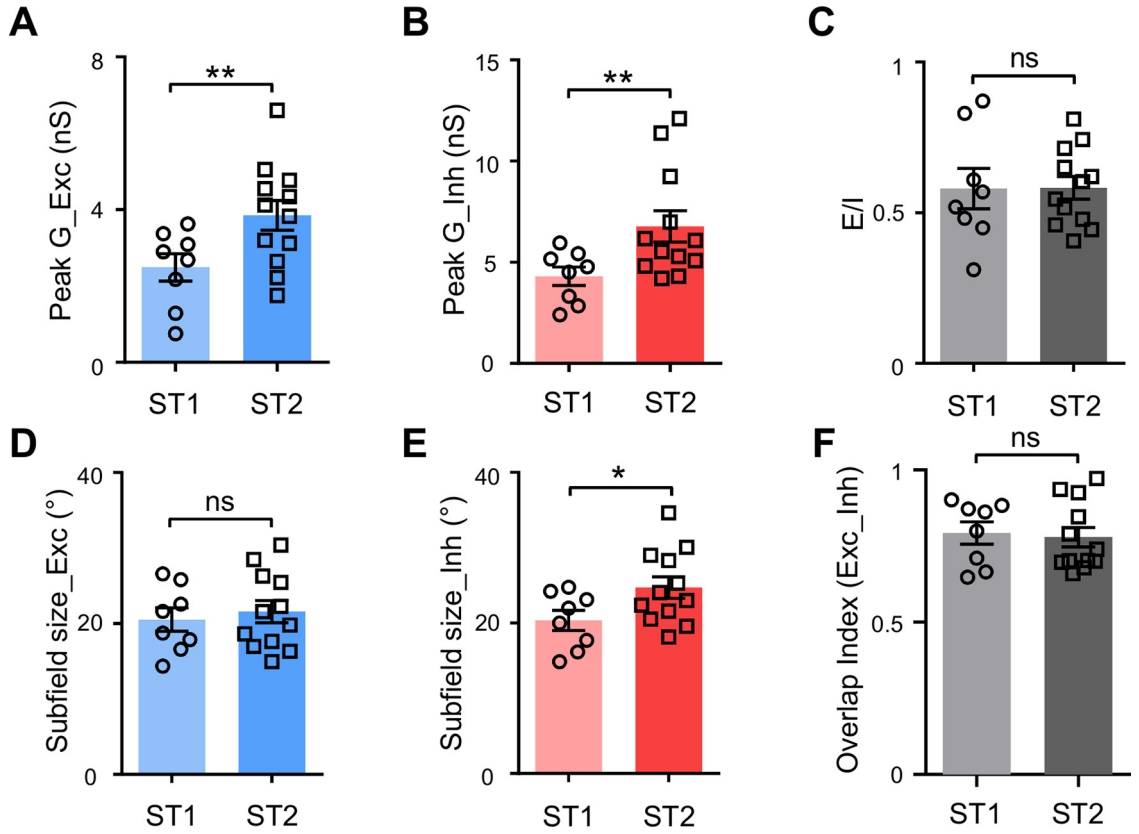

Figure 5. Changes of synaptic response properties during development. ***A***, Comparison of the maximum peak conductance of excitatory responses (averaged) to a flashing square within the RF between two stages (ST1, 2.5 ± 1.0 nS; ST2, 3.8 ± 1.3 nS; $^{**}p = 0.0097$, two-sample *t* test, $n = 10$ and 14 cells, respectively. ***B***, Comparison of the maximum peak conductance of inhibitory responses within the RF (ST1, 4.3 ± 1.3 nS; ST2, 6.8 ± 2.7 nS; $^{**}p = 0.0072$, two-sample *t* test, $n = 10$ and 14 cells, respectively. ***C***, Excitation-to-inhibition (E/I) ratio (ST1, 0.58 ± 0.19; ST2, 0.58 ± 0.13; $p = 0.49$, two-sample *t* test, $n = 10$ and 14 cells, respectively. ***D***, Comparison of dominant excitatory subfield sizes (ST1, 20.5° ± 4.4°; ST2, 21.6° ± 5.1°; $p = 0.31$, two-sample *t* test, $n = 8$ and 12 cells, respectively. ***E***, Comparison of dominant inhibitory subfield sizes (ST1, 20.3° ± 3.8°; ST2, 24.8° ± 4.9°; $^{*}p = 0.019$, two-sample *t* test, $n = 8$ and 12 cells, respectively. ***F***, Overlap index calculated between the excitatory and inhibitory subfields of the same sign (ST1, 0.79 ± 0.10; ST2, 0.78 ± 0.11; $p = 0.39$, two-sample *t* test, $n = 8$ and 12 cells, respectively. Error bar indicates SEM for all.

the experimentally obtained excitatory and inhibitory conductances (Fig. 6*G*, top). We found that neurons at ST2 tended to have larger PSPs than those at ST1 (21.0 ± 3.8 mV vs 18.0 ± 5.5 mV; Fig. 6*G*). Among the ST1 neurons, only 38% of them (3/8 cells) had a peak PSP that surpassed the presumed spiking threshold of 20 mV, whereas 67% of ST2 neurons (8/12 cells) did so (Fig. 6*H*). Moreover, the predicted firing rate tended to be lower at ST1 than at ST2 (Fig. 6*I*), consistent with the experimental observation of higher evoked firing rates at ST2. Therefore, the observed balanced enhancement of excitatory and inhibitory synaptic inputs can directly contribute to the increased responses and RF detectability of layer 4 neurons during development.

The reduction of spontaneous activity contributes to the increased RF detection

In addition to the synaptic input changes, the observed reduction of spontaneous firing rates could also influence how well a spatially organized RF can be detected. As shown in a schematic illustration (Fig. 6*J*, top), a reduction of the spontaneous firing rate alone can lower the detection threshold for evoked responses, equivalent to lowering the effective spike threshold, and therefore enhances the detection of a spatially organized RF. By random sampling from a large pool of evoked firing rates consistent with experimental observations (see above, Materials and Methods), we examined how the detection probability depended on the spontaneous firing rate. Detection rate was increased with increasing SNR, and the spontaneous firing rate at the ST2 level shifted the curve leftward relative to that at the ST1 level (Fig. 6*J*, bottom). Therefore, with the reduced spontaneous firing rate and enhanced SNR at ST2, the detection probability could be greatly enhanced. This result demonstrates that the reduction of spontaneous activity per se is an important factor contributing to the maturation of RFs.

Effects of dark rearing on the development of visual RFs

Previous studies have demonstrated that in excitatory neurons of mouse visual cortex orientation selectivity develops more or less normally when visual experience is deprived by DR (Wang et al., 2010; Kuhlman et al., 2011; Rochefort et al., 2011; Li et al., 2012; Ko et al., 2014; Sarnaik et al., 2014; Jenks and Shepherd, 2020). To examine whether visual experience is similarly dispensable for the development of RFs, we reared animals in total darkness from P9 and examined spiking and synaptic responses to bright and dark squares at P21–P28 (after DR, comparable to ST2). We found a similar trend of response level changes to the normal development; compared with those at ST1, spontaneous firing rate was significantly reduced after DR (Fig. 7*A*; $p < 0.001$, one-way ANOVA and *post hoc* test), whereas evoked firing rate was noticeably increased (Fig. 7*B*; $p = 0.014$, one-way ANOVA and *post hoc* test), and thus SNR was enhanced (Fig. 7*C*; $p < 0.001$, one-way ANOVA and *post hoc* test). In addition, the proportion of cells showing a clear RF was significantly higher than that at

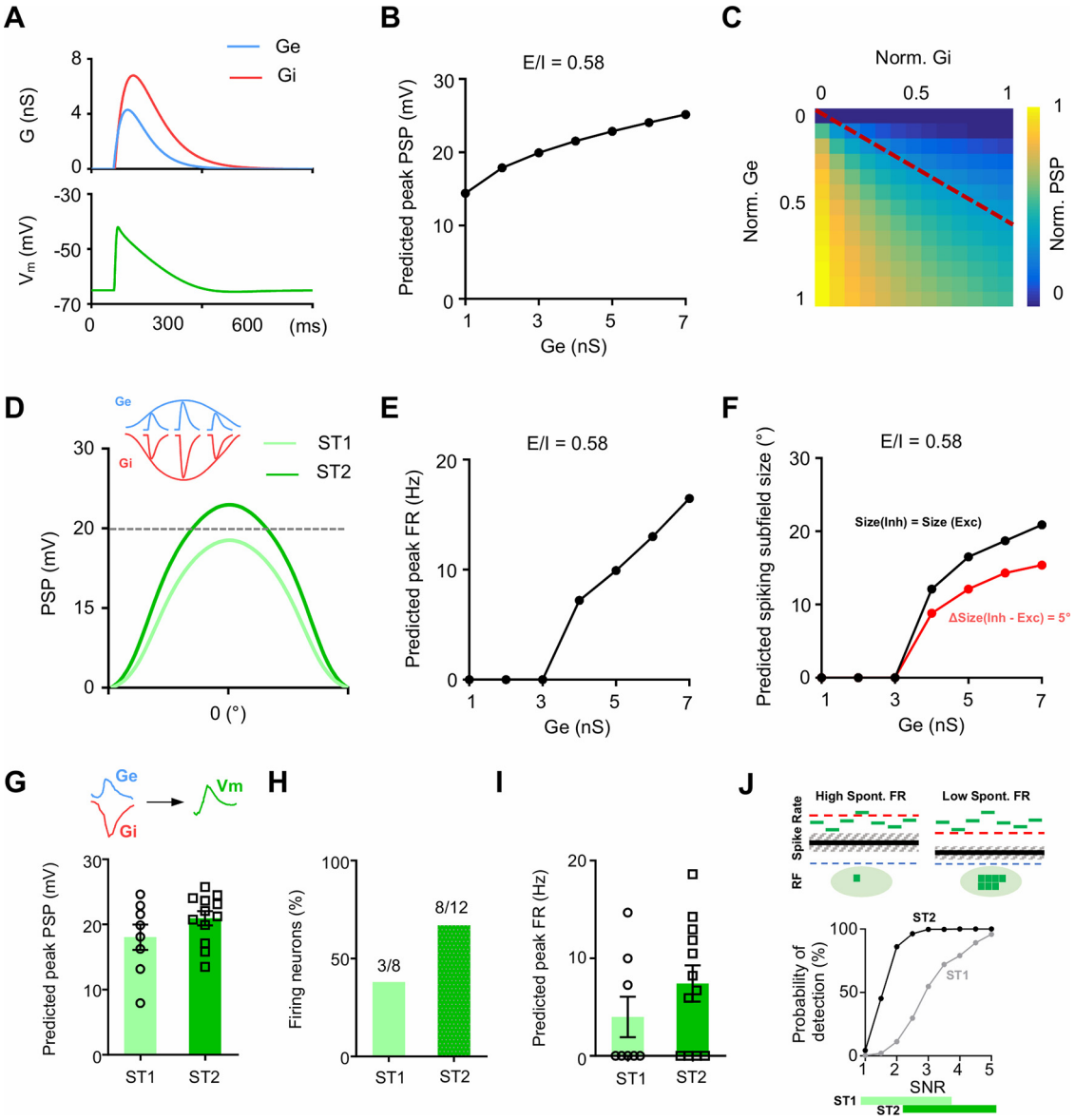

Figure 6. Neuron modeling to simulate membrane potential and subfield size changes during development. ***A***, Top, Simulated square stimulus-evoked excitatory (Ge) and inhibitory (Gi) synaptic conductances of the neuron (top) and the derived membrane potential response using the single-compartment neuron model (bottom). ***B***, Change of the peak PSP response with increasing excitatory conductances (*E*) under a constant E/I ratio of 0.58, the average value observed experimentally at both ST1 and ST2. ***C***, Color-coded amplitudes of PSPs at various combinations of E/I strengths. The maximum conductance is 12.1 nS. Red dashed line marks the trajectory of E/I ratio = 0.58. ***D***, Spatial tuning of PSP responses at two different stages. Dashed line marks the presumed 20 mV spike threshold. Inset, Schematic spatial tuning of excitation (blue) and inhibition (red) and sample synaptic conductances at the corresponding locations. In this stimulation, the spatial tuning of synaptic conductances was kept the same between ST1 and ST2, whereas the response amplitude (for both excitation and inhibition) was increased from ST1 to ST2, keeping the E/I ratio the same. ***E***, Predicted evoked firing rate with increasing excitation amplitudes under a constant E/I ratio of 0.58. ***F***, Predicted spike subfield size with increasing excitation amplitudes under a constant E/I ratio of 0.58. Black line indicates that excitatory and inhibitory subfield sizes are equal. Red line indicates inhibitory subfield is 5° larger than the excitatory subfield as observed experimentally at ST2. ***G***, Peak PSP amplitudes derived by integrating experimentally obtained excitatory and inhibitory inputs with the neuron model (ST1, 18.0 ± 5.5 mV; ST2, 21.0 ± 3.8 mV; $p = 0.11$, two-sample *t* test, $n = 8$ and 12 cells, respectively. Top, Example of experimentally obtained excitatory and inhibitory conductances in a cell responding to the same flash square (left) and the derived PSP response [membrane potential (Vm), right]. ***H***, Percentage of neurons with PSPs surpassing a spike threshold of 20 mV at two stages. ***I***, Predicted evoked firing rates of neurons at ST1 versus ST2 based on a power law function (ST1, 3.9 ± 5.8 Hz; ST2, 7.4 ± 6.4 Hz; $p = 0.14$, two-sample *t* test, $n = 8$ and 12 cells, respectively). The firing rates of neurons with PSPs lower than 20 mV were set as zero. Error bar indicates SEM. ***J***, Top, Illustration of the influence of spontaneous firing rate on detectability of RFs. The black line and gray shaded area represent the mean and SD of spontaneous firing rate, respectively, with the blue dash line labeling spike rate = 0. The green bar represents the spike rate to a square stimulus within the subthreshold RF (represented by the light green eclipse). Red dashed line marks the detection threshold (mean + 3 SD). Solid green squares mark visual stimuli that result in the detection of a significant evoked response. Bottom, detection probability (see above, Materials and Methods) plotted against SNR. The two curves are generated by using spontaneous firing rates at ST1 and ST2 levels, respectively. Colored bars depict the range of SNR at ST1 and ST2, respectively (Note that the ST2 range has been cut off at 5 because the mean value is much higher than 5.).

ST1 (Fig. 7*D*; DR vs ST1, 73 vs 20%, $p < 0.001$, Fisher's exact test). These data demonstrate that despite the deprivation of vision, the development of RFs proceeds relatively well, suggesting that a large component of RF development is experience independent. However, comparing to normally reared (NR) animals at ST2, we did find a significant reduction in both the spontaneous (Fig. 7*A*; $p = 0.024$, one-way ANOVA and *post hoc* test) and evoked firing rates (Fig. 7*B*; $p = 0.0024$, one-way ANOVA and *post hoc* test) as well as in the proportion of cells showing a clear RF (Fig. 7*D*; DR vs ST2, 73 vs 90%, $p < 0.001$,

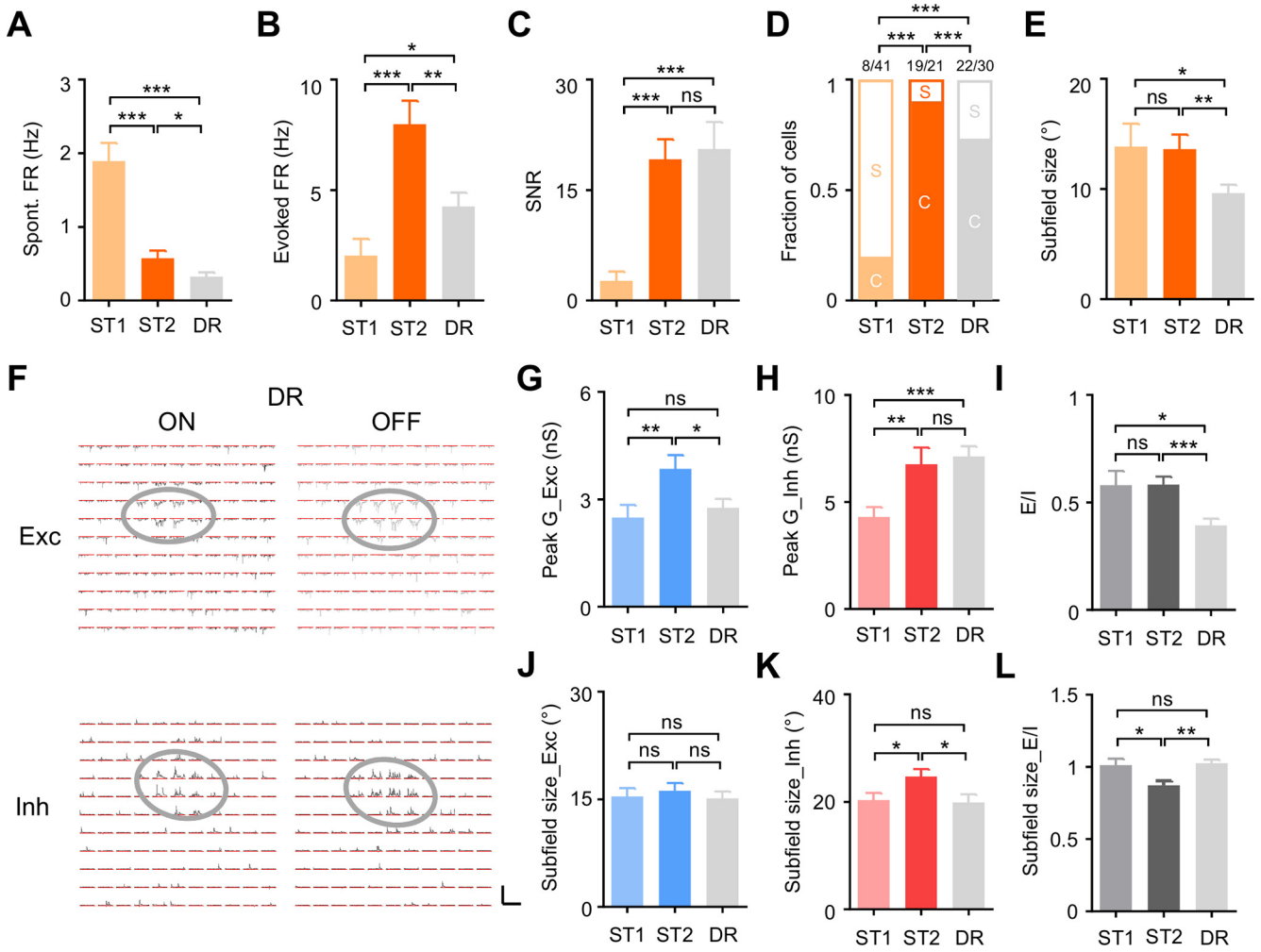

Figure 7. Effects of dark rearing on the development of spiking and synaptic RFs. ***A–C***, Spontaneous firing rates (***A***), evoked firing rates (***B***), and SNR (***C***) of neurons at ST1 ($n = 41$ cells) or ST2 ($n = 21$ cells) during normal development versus after DR ($n = 30$ cells). Statistics are the following: spontaneous firing rates (DR, 0.3 ± 0.3 Hz; ST1 vs DR, $p < 0.001$; ST2 vs DR, $p = 0.024$), evoked firing rates (DR, 4.3 ± 3.5 Hz; ST1 vs DR, $p = 0.014$; ST2 vs DR, $p = 0.0024$), and SNR (DR, 20.5 ± 20.2; ST1 vs DR, $p < 0.001$; ST2 vs DR, $p = 0.38$), one-way ANOVA and *post hoc* test. ***D***, Fractions of clear (C) versus sluggish (S) RFs at ST1, ST2, and after DR, respectively (***$p < 0.001$, Fisher's exact test; $n = 41$, 21, and 30 cells, respectively). ***E***, Dominant subfield sizes of cells at ST1 ($n = 8$ cells) or ST2 ($n = 19$ cells) versus after DR ($n = 22$ cells; DR, 9.6° ± 3.6°; ST1 vs DR, $p = 0.046$; ST2 vs DR, $p = 0.0078$; one-way ANOVA and *post hoc* test). ***F***, Excitatory and inhibitory ON/OFF subfields of an example layer 4 neuron after DR. Gray ellipses delineate the subfield boundary. Scale bar, 300 pA and 300 ms. ***G–I***, Peak evoked excitatory (***G***) and inhibitory (***H***) conductances and E/I ratio (***I***) of the cells at ST1 ($n = 10$ cells) or ST2 ($n = 12$ cells) versus after DR ($n = 13$ cells). Statistics are the following: excitatory conductance (DR, 2.8 ± 0.9 nS; ST1 vs DR, $p = 0.27$; ST2 vs DR, $p = 0.015$), inhibitory conductance (DR, 7.1 ± 1.7 nS; ST1 vs DR, $p < 0.001$; ST2 vs DR, $p = 0.35$), and E/I ratio (DR, 0.40 ± 0.11; ST1 vs DR, $p = 0.015$; ST2 vs DR, $p < 0.001$); one-way ANOVA and *post hoc* test. ***J–L***, Excitatory subfield size (***J***), inhibitory subfield size (***K***), and the ratio of excitatory over inhibitory subfield sizes (***L***) of the cells at ST1 ($n = 8$ cells) or ST2 ($n = 12$ cells) versus after DR ($n = 13$ cells). Statistics are the following: excitatory subfield size (DR, 20.1° ± 4.6°; ST1 vs DR, $p = 0.43$; ST2 vs DR, $p = 0.24$), inhibitory subfield size (DR, 19.9° ± 5.3°; ST1 vs DR, $p = 0.41$; ST2 vs DR, $p = 0.015$), and excitatory-to-inhibitory subfield size ratio (DR, 1.03 ± 0.09; ST1 vs DR, $p = 0.40$; ST2 vs DR, $p < 0.001$); ***$p < 0.001$, **$p < 0.01$, *$p < 0.05$; one-way ANOVA and *post hoc* test. Error bar indicates SEM.

Fisher's exact test). For these cells, 41% (9/22) had ON-OFF RFs, 9% (2/22) had an ON only, and 50% (11/22) had an OFF-only RF (DR vs ST2, $p = 0.33$, χ^2 test). In addition, the dominant subfield size was reduced after DR compared with both ST1 and ST2 of normal development (Fig. 7*E*; ST1 vs DR, $p = 0.046$; ST2 vs DR, $p = 0.0078$, one-way ANOVA and *post hoc* test). These results suggest that DR does interfere in some aspects of RF development, possibly through altering the excitation/inhibition balance.

We next sought to investigate synaptic mechanisms underlying the reduction of response level and subfield shrinkage after DR, using whole-cell voltage-clamp recording. The input resistance of cells recorded in DR mice was not different from that of ST2 cells in NR animals (315 ± 78 MΩ vs 292 ± 57 MΩ, $p = 0.51$, *t* test; $n = 13$ and 12 cells, respectively). We found that excitatory and inhibitory synaptic subfields remained well spatially defined (13 of 13 cells) and were seemingly normal in shape after DR (Fig. 7*F*, gray ovals). However, a closer examination revealed an impedance of subfield development caused by DR; the excitatory input was underdeveloped and remained as weak as that at ST1 (Fig. 7*G*; ST1 vs DR, $p = 0.27$; ST2 vs DR, $p = 0.015$, one-way ANOVA and *post hoc* test), whereas the inhibitory input appeared normally developed in strength (Fig. 7*H*, ST1 vs DR, $p < 0.001$; ST2 vs DR, $p = 0.35$, one-way ANOVA and *post hoc* test). This unbalanced development led to a significant reduction of the E/I ratio (Fig. 7*I*; ST1 vs DR, $p = 0.015$; ST2 vs DR, $p < 0.001$, one-way ANOVA and *post hoc* test), that is, relatively more dominance of inhibition over excitation after DR, which may explain the suppression of both spontaneous and evoked firing rates. Additionally, although the excitatory subfield size was not affected (Fig. 7*J*; ST2 vs DR, $p = 0.43$, one-way ANOVA and *post hoc* test), the developmental broadening of the inhibitory

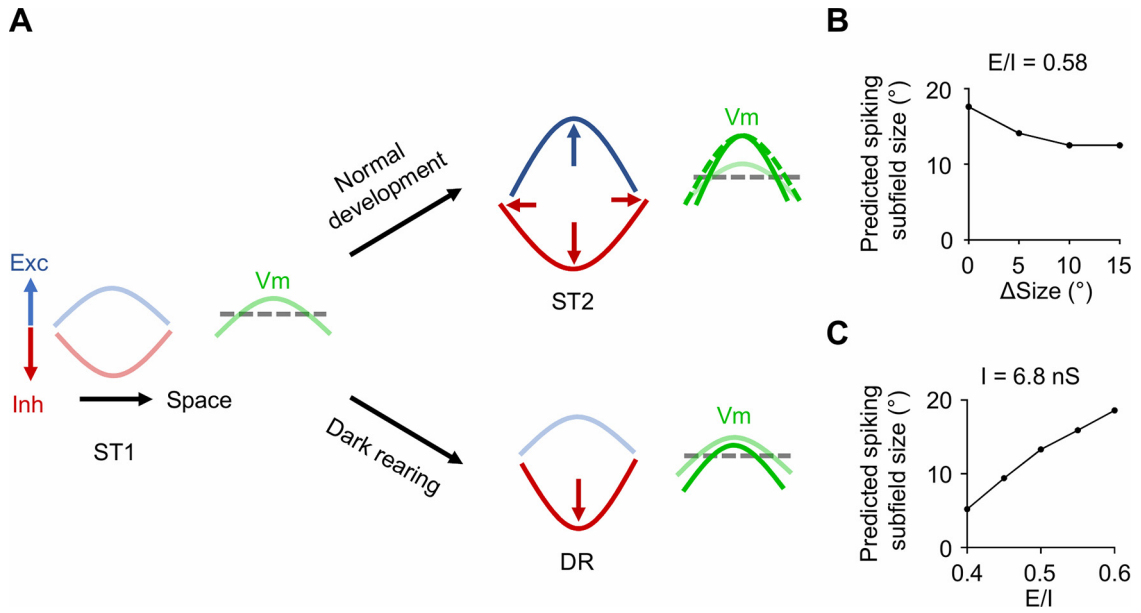

Figure 8. A working model for the maturation of RF during development. ***A***, Blue, red, and green curves represent the spatial tuning (or RF subfield) of excitation, inhibition, and membrane potential (Vm) responses, respectively. Gray dashed line represents the spike threshold. At ST1, the premature excitation and inhibition result in relatively weak Vm responses (pale green) and only suprathreshold Vm responses (or spike responses that are above the detection threshold) in a small fraction of neurons. Under normal development at ST2, the amplitudes of excitation and inhibition are enhanced in proportion (vertical arrows), and the inhibitory subfield is broadened (horizontal arrows), resulting in stronger suprathreshold Vm responses and emergence of a distinct spike subfield (bright green). Note that without the developmental broadening of the inhibitory RF, the resultant spike subfield would be broadened (compare dashed green and solid green lines). Under DR, the maturation of excitation is arrested, while inhibition enhances its strength to the mature state (red vertical arrow) without broadening its spatial tuning. This unbalanced change of inhibition results in reduced Vm responses (bright green, compared with pale green). Note that spontaneous firing rate is reduced after DR, equivalent to lowering the detection threshold. Together, these effects lead to a smaller spike subfield. ***B***, Simulation of the effect of the developmental broadening of inhibitory subfield on the spike subfield size (see above, Materials and Methods). ΔSize is the difference between inhibitory and excitatory subfield sizes, whereas the peak amplitudes of excitation and inhibition (E/I ratio = 0.58) as well as the excitatory subfield size are kept the same. The maximum conductances of excitation and inhibition are 4.3 and 6.8 nS, respectively. Note that the mean experimentally observed ΔSize at ST2 is 5°. ***C***, Simulation of the effect of impaired maturation of excitation and reduced spontaneous firing rates on the spike subfield size after DR (see above, Materials and Methods). The peak amplitude of inhibition (6.8 nS) as well as the inhibitory and excitatory subfield sizes are kept the same, whereas the amplitude of excitation (therefore, E/I ratio) is varied.

subfield was prevented by DR (Fig. 7*K*; ST2 vs DR, $p = 0.015$, one-way ANOVA and *post hoc* test). Thus, the ratio of excitatory over inhibitory subfield size was substantially increased compared with ST2 but remained the same as ST1 (Fig. 7*L*; ST1 vs DR, $p = 0.40$; ST2 vs DR, $p < 0.001$, one-way ANOVA and *post hoc* test). On the other hand, the spatial overlap between excitatory and inhibitory subfields (of the same sign) was not affected by DR (OI after DR, 0.78 ± 0.096; DR vs ST2, $p = 0.47$, *t* test). Together, these data indicate that DR results in abnormal underdevelopment of excitation and paradoxically normal development of inhibition, leading to abnormal dominance of inhibition over excitation.

Discussion

A proper spatial organization of RFs is fundamental for normal visual function (Priebe and Ferster, 2012; Niell, 2015). However, how the RF structure matures during development and what the underlying changes of synaptic inputs are remain not well understood. In the present study, we found that premature V1 layer 4 neurons around eye opening rarely exhibited spatially organized visual RFs at the spike level, whereas clear RFs were observed in most of neurons 1–2 weeks after. In accompany with this RF maturation, spontaneous firing rates were reduced while evoked firing rates were increased, leading to a robust enhancement of SNR of visual responses within the RF.

The suppression of high spontaneous activity is consistent with the notion of an increasing inhibitory tone during post-eye-opening development (Morales et al., 2002; Chattopadhyaya et al., 2004). The developmental trends of decreases in spontaneous firing rates and increases in visually evoked responses generally agree with the results of several previous studies (Li et al., 2012; Hoy and Niell, 2015; Roy et al., 2020), although they have not reached statistical significance in layer 4 in one study (Hoy and Niell, 2015). The decrease in the spontaneous firing rate and the increase in SNR together contribute importantly to the increased detectability of RFs (Fig. 6*J*). These changes may similarly contribute to the developmental increase in the fraction of visually responsive neurons reported previously (Hoy and Niell, 2015; Jenks and Shepherd, 2020). Therefore, it is possible that SNR could be a critical indicator of maturation status of cortical neurons. It should be noted that early neurons without exhibiting a clear RF may still be responsive to other stimulation patterns such as full-field moving gratings, leading to an apparently higher fraction of overall visually responsive neurons (Hoy and Niell, 2015) than the fraction reported here.

Different from the spike RF, we found that synaptic RFs (both excitatory and inhibitory) were mostly clear cut at the earliest post-eye-opening stage. The largely overlapping patterns of excitatory and inhibitory subfields are similar to what has been found in the adult cortex (Liu et al., 2010). This indicates that spatial RFs of thalamic relay neurons are already formed (Davis et al., 2015; Tschetter et al., 2018) and that the basic thalamocortical wiring pattern is already established around eye opening, likely under the influence of cortical/subcortical activity driven by spontaneous retinal waves (Katz and Shatz, 1996; Blankenship and Feller, 2010). This notion is also supported by observations that several visual functions such as orientation and direction

selectivity are already present at the time of eye opening (Wang et al., 2010; Kuhlman et al., 2011; Rochefort et al., 2011; Li et al., 2012; Ko et al., 2014). Nevertheless, both excitatory and inhibitory inputs undergo robust developmental changes after the onset of visual experience (Fig. 8*A*). On a global scale, excitation and inhibition were scaled up in a balanced manner, as the E/I ratio of visually evoked synaptic conductances was constant during development. Such a balanced enhancement of excitatory and inhibitory synaptic strengths can help to increase evoked firing rates while preventing response saturation (Pouille et al., 2009; Liu et al., 2011). However, simply upregulating excitation and inhibition would generally lead to a reduction of tuning strength (Liu et al., 2011; Li et al., 2012), specifically in this study to enlarged spike subfields. Fortunately, inhibitory subfield size was increased during development. Such broadening of inhibitory spatial tuning, together with the enhancement of its strength, can effectively refine the spike subfield (Fig. 6*F*) by suppressing membrane potential (and spiking) responses at RF surrounding regions, creating a clear-cut boundary. Remarkably, only moderately broader than the excitatory subfield, inhibition can already effectively sharpen the spike subfield (Fig. 8*B*). These modeling results are reminiscent of previous demonstrations that inhibition more broadly tuned than excitation can sharpen orientation selectivity in the face of weakly tuned excitation (Somers et al., 1995; Liu et al., 2011) and that broadening of inhibitory orientation tuning can lead to developmental sharpening of orientation selectivity (Li et al., 2012).

Different from the inhibitory subfield, the excitatory subfield remained unchanged in size. A previous study in the mouse dorsal lateral geniculate nucleus (dLGN) has shown that the spatial RF of thalamic relay neurons is reduced in size by half during development (Tschetter et al., 2018), which is attributable to reduced convergence (i.e., pruning) of retinogeniculate connections (Litvina and Chen, 2017; Tschetter et al., 2018). The unchanged excitatory subfield size in layer 4 thus suggests that the number of dLGN neurons connecting to a layer 4 neuron might be increased after eye opening, which can also contribute to the increased excitatory (and inhibitory) input strength. In this sense, retinogeniculate and geniculocortical connectivity might be developmentally regulated in an opposite manner. In addition, as layer 4 is the major thalamo-recipient layer of V1, changes of both feedforward thalamocortical and recurrent intracortical connectivity (Ko et al., 2013) can contribute to the developmental change of excitatory input. It will be of great interest to know how each of these components can account for the developmental maturation of the RF structure (Sun et al., 2019).

In addition to the synaptic input changes, any possible changes of intrinsic membrane properties of neurons can influence the detectability of spike RFs. A previous slice recording study of pyramidal neurons in the rat prefrontal cortex has reported only minor or negligible changes in input resistance, membrane time constant, and spike threshold after eye opening (Zhang, 2004). Consistently, we did not find a significant difference in input resistance between ST1 and ST2 cells. Nevertheless, we do not exclude the possibility that changes of other membrane properties, for example, lowering of the spike threshold (Roy et al., 2020), can further contribute to the increased salience of visually evoked activity and detectability of RFs.

Sensory experience is required for various aspects of normal visual functional development in the cortex during the critical period (Fagiolini et al., 1994; White et al., 2001; Wang et al., 2010; Kuhlman et al., 2011; Li et al., 2012; Sarnaik et al., 2014). Indeed, in this study, our data demonstrate that both the spontaneous and evoked firing rates as well as spike subfield sizes were diminished after DR, suggesting an overall reduction of responsiveness, which is in agreement with a number of previous studies (Braastad and Heggelund, 1985; Tsumoto and Freeman, 1987; Fagiolini et al., 1994; Tropea et al., 2010). A later study, however, reports no significant change in the overall RF size (i.e., considering both ON and OFF subfields) in slightly older (P31–P35) DR mice compared with the NR control (Sarnaik et al., 2014). On the one hand, DR effects could be dependent on when and for how long it is applied (Benevento et al., 1992). On the other hand, the above observation may be in fact in line with our result of unaffected excitatory subfield sizes, considering that ON/OFF synaptic subfields are largely overlapping. Despite the largely normal development of monocular RFs, the development of spatial acuity as measured behaviorally is significantly delayed by DR (Kang et al., 2013), possibly because the acuity examined under binocular conditions is affected by binocular matching of monocular RF properties, which is affected by DR (Sarnaik et al., 2014).

The change in spike subfield sizes can be explained by the imbalanced changes of synaptic strengths; excitation remained weak and not strengthened, whereas inhibition underwent apparently normal developmental strengthening, creating an abnormal dominance of inhibition over excitation and resulting in reduced subfield sizes (Fig. 8*C*). The underdevelopment of excitation is likely a result of combined effects, that is, delayed pruning of retinogeniculate synapses (Hooks and Chen, 2008) and a delayed increase in the convergence of thalamocortical synapses. The relatively enhanced inhibition is consistent with previous *in vitro* slice recording results showing that inhibitory synaptic transmission in layer 4 is potentiated after sensory deprivation (Maffei et al., 2006; Nahmani and Turrigiano, 2014). This paradoxical enhancement of inhibition may be attributed to a compensatory recruitment of more inhibitory inputs and/or strengthening of presynaptic and postsynaptic functions of inhibitory synapses during DR (Maffei et al., 2006; Nahmani and Turrigiano, 2014; Miao et al., 2016). Combined thalamocortical and intracortical effects may lead to the failed enlargement of inhibitory subfields after DR. It is worth noting that some of DR effects on inhibition might be masked as it has been shown previously in layer 2/3 pyramidal neurons that restoring vision after DR only for a short period of time (2 h, comparable to our time window for visual stimulation) can partially reverse some DR effects on miniature inhibitory postsynaptic currents (Gao et al., 2014). Finally, studies have suggested that the impact of parvalbumin (PV) and somatostatin inhibitory neurons on pyramidal cells is increased and decreased, respectively, during a similar developmental window to this study (Miao et al., 2016; Yaeger et al., 2019) and that the development of PV-neuron function is regulated by visual experience (Kuhlman et al., 2011; Li et al., 2012). How the inhibitory-neuron subtypes contribute distinctly to the experience-dependent RF maturation awaits further investigations.

References

Benevento LA, Bakkum BW, Port JD, Cohen RS (1992) The effects of dark-rearing on the electrophysiology of the rat visual cortex. Brain Res 572:198–207.

Berardi N, Pizzorusso T, Maffei L (2000) Critical periods during sensory development. Curr Opin Neurobiol 10:138–145.

Blankenship AG, Feller MB (2010) Mechanisms underlying spontaneous patterned activity in developing neural circuits. Nat Rev Neurosci 11:18–29.

Braastad BO, Heggelund P (1985) Development of spatial receptive-field organization and orientation selectivity in kitten striate cortex. J Neurophysiol 53:1158–1178.

Cang J, Feldheim DA (2013) Developmental mechanisms of topographic map formation and alignment. Annu Rev Neurosci 36:51–77.
Carandini M, Ferster D (2000) Membrane potential and firing rate in cat primary visual cortex. J Neurosci 20:470–484.
Chang JT, Whitney D, Fitzpatrick D (2020) Experience-dependent reorganization drives development of a binocularly unified cortical representation of orientation. Neuron 107:338–350.e5.
Chapman B, Stryker MP (1993) Development of orientation selectivity in ferret visual cortex and effects of deprivation. J Neurosci 13:5251–5262.
Chattopadhyaya B, Di Cristo G, Higashiyama H, Knott GW, Kuhlman SJ, Welker E, Huang ZJ (2004) Experience and activity-dependent maturation of perisomatic GABAergic innervation in primary visual cortex during a postnatal critical period. J Neurosci 24:9598–9611.
Chou X-L, Fang Q, Yan L, Zhong W, Peng B, Li H, Wei J, Tao HW, Zhang LI (2020) Contextual and cross-modality modulation of auditory cortical processing through pulvinar mediated suppression. Elife 9:e54157.
Clemens JM, Ritter NJ, Roy A, Miller JM, Van Hooser SD (2012) The laminar development of direction selectivity in ferret visual cortex. J Neurosci 32:18177–18185.
Davis ZW, Chapman B, Cheng H-J (2015) Increasing spontaneous retinal activity before eye opening accelerates the development of geniculate receptive fields. J Neurosci 35:14612–14623.
Espinosa JS, Stryker MP (2012) Development and plasticity of the primary visual cortex. Neuron 75:230–249.
Fagiolini M, Pizzorusso T, Berardi N, Domenici L, Maffei L (1994) Functional postnatal development of the rat primary visual cortex and the role of visual experience: dark rearing and monocular deprivation. Vision Res 34:709–720.
Fang Q, Chou X-L, Peng B, Zhong W, Zhang LI, Tao HW (2020) A differential circuit via retino-colliculo-pulvinar pathway enhances feature selectivity in visual cortex through surround suppression. Neuron 105:355–369.e6.
Gao M, Maynard KR, Chokshi V, Song L, Jacobs C, Wang H, Tran T, Martinowich K, Lee H-K (2014) Rebound potentiation of inhibition in juvenile visual cortex requires vision-induced BDNF expression. J Neurosci 34:10770–10779.
Gianfranceschi L, Siciliano R, Walls J, Morales B, Kirkwood A, Huang ZJ, Tonegawa S, Maffei L (2003) Visual cortex is rescued from the effects of dark rearing by overexpression of BDNF. Proc Natl Acad Sci U S A 100:12486–12491.
Hensch TK (2005) Critical period plasticity in local cortical circuits. Nat Rev Neurosci 6:877–888.
Hirsch JA, Martinez LM (2006) Circuits that build visual cortical receptive fields. Trends Neurosci 29:30–39.
Hofer SB, Mrsic-Flogel TD, Bonhoeffer T, Hübener M (2006) Lifelong learning: ocular dominance plasticity in mouse visual cortex. Curr Opin Neurobiol 16:451–459.
Hooks BM, Chen C (2008) Vision triggers an experience-dependent sensitive period at the retinogeniculate synapse. J Neurosci 28:4807–4817.
Hooks BM, Chen C (2020) Circuitry underlying experience-dependent plasticity in the mouse visual system. Neuron 106:21–36.
Hoy JL, Niell CM (2015) Layer-specific refinement of visual cortex function after eye opening in the awake mouse. J Neurosci 35:3370–3383.
Hubel DH, Wiesel TN (1970) The period of susceptibility to the physiological effects of unilateral eye closure in kittens. J Physiol 206:419–436.
Jenks KR, Shepherd JD (2020) Experience-dependent development and maintenance of binocular neurons in the mouse visual cortex. Cell Rep 30:1982–1994.e4.
Jones JP, Palmer LA (1987) The two-dimensional spatial structure of simple receptive fields in cat striate cortex. J Neurophysiol 58:1187–1211.
Kang E, Durand S, LeBlanc JJ, Hensch TK, Chen C, Fagiolini M (2013) Visual acuity development and plasticity in the absence of sensory experience. J Neurosci 33:17789–17796.
Katz LC, Shatz CJ (1996) Synaptic activity and the construction of cortical circuits. Science 274:1133–1138.
Ko H, Cossell L, Baragli C, Antolik J, Clopath C, Hofer SB, Mrsic-Flogel TD (2013) The emergence of functional microcircuits in visual cortex. Nature 496:96–100.
Ko H, Mrsic-Flogel TD, Hofer SB (2014) Emergence of feature-specific connectivity in cortical microcircuits in the absence of visual experience. J Neurosci 34:9812–9816.
Kuhlman SJ, Tring E, Trachtenberg JT (2011) Fast-spiking interneurons have an initial orientation bias that is lost with vision. Nat Neurosci 14:1121–1133.
Li Y, Fitzpatrick D, White LE (2006) The development of direction selectivity in ferret visual cortex requires early visual experience. Nat Neurosci 9:676–681.
Li Y, Van Hooser SD, Mazurek M, White LE, Fitzpatrick D (2008) Experience with moving visual stimuli drives the early development of cortical direction selectivity. Nature 456:952–956.
Li YT, Ma W-P, Pan C-J, Zhang LI, Tao HW (2012) Broadening of cortical inhibition mediates developmental sharpening of orientation selectivity. J Neurosci 32:3981–3991.
Li YT, Liu BH, Chou XL, Zhang LI, Tao HW (2015) Synaptic basis for differential orientation selectivity between complex and simple cells in mouse visual cortex. J Neurosci 35:11081–11093.
Li YT, Fang Q, Zhang LI, Tao HW (2018) Spatial asymmetry and short-term suppression underlie direction selectivity of synaptic excitation in the mouse visual cortex. Cereb Cortex 28:2059–2070.
Litvina EY, Chen C (2017) Functional convergence at the retinogeniculate synapse. Neuron 96:330–338.e5.
Liu B, Li P, Sun YJ, Li Y, Zhang LI, Tao HW (2010) Intervening inhibition underlies simple-cell receptive field structure in visual cortex. Nat Neurosci 13:89–96.
Liu B, Li Y, Ma W, Pan C, Zhang LI, Tao HW (2011) Broad inhibition sharpens orientation selectivity by expanding input dynamic range in mouse simple cells. Neuron 71:542–554.
Liu BH, Li P, Li YT, Sun YJ, Yanagawa Y, Obata K, Zhang LI, Tao HW (2009) Visual receptive field structure of cortical inhibitory neurons revealed by two-photon imaging guided recording. J Neurosci 29:10520–10532.
Ma WP, Li YT, Tao HW (2013) Downregulation of cortical inhibition mediates ocular dominance plasticity during the critical period. J Neurosci 33:11276–11280.
Maffei A, Nataraj K, Nelson SB, Turrigiano GG (2006) Potentiation of cortical inhibition by visual deprivation. Nature 443:81–84.
Miao Q, Yao L, Rasch MJ, Ye Q, Li X, Zhang X (2016) Selective maturation of temporal dynamics of intracortical excitatory transmission at the critical period onset. Cell Rep 16:1677–1689.
Moore BD, Freeman RD (2012) Development of orientation tuning in simple cells of primary visual cortex. J Neurophysiol 107:2506–2516.
Morales B, Choi SY, Kirkwood A (2002) Dark rearing alters the development of GABAergic transmission in visual cortex. J Neurosci 22:8084–8090.
Nahmani M, Turrigiano GG (2014) Deprivation-induced strengthening of presynaptic and postsynaptic inhibitory transmission in layer 4 of visual cortex during the critical period. J Neurosci 34:2571–2582.
Niell CM (2015) Cell types, circuits, and receptive fields in the mouse visual cortex. Annu Rev Neurosci 38:413–431.
Petrus E, Rodriguez G, Patterson R, Connor B, Kanold PO, Lee HK (2015) Vision loss shifts the balance of feedforward and intracortical circuits in opposite directions in mouse primary auditory and visual cortices. J Neurosci 35:8790–8801.
Pouille F, Marin-Burgin A, Adesnik H, Atallah BV, Scanziani M (2009) Input normalization by global feedforward inhibition expands cortical dynamic range. Nat Neurosci 12:1577–1585.
Priebe NJ, Ferster D (2012) Mechanisms of neuronal computation in mammalian visual cortex. Neuron 75:194–208.
Rochefort NL, Narushima M, Grienberger C, Marandi N, Hill DN, Konnerth A (2011) Development of direction selectivity in mouse cortical neurons. Neuron 71:425–432.
Roy A, Osik JJ, Meschede-Krasa B, Alford W, Leman DP, Van Hooser SD (2020) Synaptic and intrinsic mechanisms underlying development of cortical direction selectivity. Elife 9:e58509.
Sarnaik R, Wang B-S, Cang J (2014) Experience-dependent and independent binocular correspondence of receptive field subregions in mouse visual cortex. Cereb Cortex 24:1658–1670.
Shatz CJ, Stryker MP (1978) Ocular dominance in layer IV of the cat's visual cortex and the effects of monocular deprivation. J Physiol 281:267–283.
Smith GB, Sederberg A, Elyada YM, Van Hooser SD, Kaschube M, Fitzpatrick D (2015) The development of cortical circuits for motion discrimination. Nat Neurosci 18:252–261.
Smith IT, Townsend LB, Huh R, Zhu H, Smith SL (2017) Stream-dependent development of higher visual cortical areas. Nat Neurosci 20:200–208.

Somers DC, Nelson SB, Sur M (1995) An emergent model of orientation selectivity in cat visual cortical simple cells. J Neurosci 15:5448–5465.

Stephany C-É, Ma X, Dorton HM, Wu J, Solomon AM, Frantz MG, Qiu S, McGee AW (2018) Distinct circuits for recovery of eye dominance and acuity in murine amblyopia. Curr Biol 28:1914–1923.e5.

Sun YJ, Liu BH, Tao HW, Zhang LI (2019) Selective strengthening of intracortical excitatory input leads to receptive field refinement during auditory cortical development. J Neurosci 39:1195–1205.

Tan L, Tring E, Ringach DL, Zipursky SL, Trachtenberg JT (2020) Vision changes the cellular composition of binocular circuitry during the critical period. Neuron 108:735–747.

Trachtenberg JT (2015) Competition, inhibition, and critical periods of cortical plasticity. Curr Opin Neurobiol 35:44–48.

Tropea D, Majewska AK, Garcia R, Sur M (2010) Structural dynamics of synapses in vivo correlate with functional changes during experience-dependent plasticity in visual cortex. J Neurosci 30:11086–11095.

Tschetter WW, Govindaiah G, Etherington IM, Guido W, Niell CM (2018) Refinement of spatial receptive fields in the developing mouse lateral geniculate nucleus is coordinated with excitatory and inhibitory remodeling. J Neurosci 38:4531–4542.

Tsumoto T, Freeman RD (1987) Dark-reared cats: responsitivity of cortical cells influenced pharmacologically by an inhibitory antagonist. Exp Brain Res 65:666–672.

Wang L, Liu M, Segraves MA, Cang J (2015) Visual experience is required for the development of eye movement maps in the mouse superior colliculus. J Neurosci 35:12281–12286.

Wang BS, Sarnaik R, Cang J (2010) Critical period plasticity matches binocular orientation preference in the visual cortex. Neuron 65:246–256.

White LE, Fitzpatrick D (2007) Vision and cortical map development. Neuron 56:327–338.

White LE, Coppola DM, Fitzpatrick D (2001) The contribution of sensory experience to the maturation of orientation selectivity in ferret visual cortex. Nature 411:1049–1052.

Yaeger CE, Ringach DL, Trachtenberg JT (2019) Neuromodulatory control of localized dendritic spiking in critical period cortex. Nature 567:100–104.

Zhang ZW (2004) Maturation of layer V pyramidal neurons in the rat prefrontal cortex: intrinsic properties and synaptic function. J Neurophysiol 91:1171–1182.